



UDC 528.835

## ESTIMATION OF LAND SURFACE TEMPERATURE BASED ON GIS AND REMOTE SENSING DATA IN DAHUK CITY

 Nabaa FALIH NASER<sup>✉</sup>, Israa FADHIL IBRAHEEM, Mufid AIHADITHI, Fatim JANAN YOSIEF

*Technical Engineering College, Middle Technical University, Baghdad, Iraq*

### Article History:

- received 08 September 2023
- accepted 04 March 2025

**Abstract.** Land Surface Temperature (LST) is a crucial variable across various domains, including studies on the global ramifications of climate change, urban land use and cover, and geo- and biophysical modelling. Satellite data from Landsat 8, specifically the NIR channel, was utilized to generate LST maps, NDVI, and LU/LC for Dahuk City. The correctness of LULC maps was verified by ground observation locations. The results indicate that the LST ranged from 4 to 14 degrees Celsius in 2013 and from 10 to 20 degrees Celsius in 2023. The highest temperatures, ranging from 14 to 20 degrees Celsius, occur in urban areas, whilst the lowest temperatures, recorded in 2013 and 2023, are in forests and aquatic environments, measuring 4 and 10 degrees Celsius, respectively and this occurred because of unplanned expansion of urban areas on behalf of green area as indicated by NDVI. Through this study planners and decision making could predict the future increase in LST if no action taken against these activities.

**Keywords:** Land Surface Temperature (LST), land use/land cover, Normalized Difference Vegetation Index (NDVI), GIS, Landsat 8 Satellite, Dahuk, Iraq.

<sup>✉</sup>Corresponding author. E-mail: [nabaatcb@mtu.edu.iq](mailto:nabaatcb@mtu.edu.iq)

### 1. Introduction

The planetary boundary layer's integrated thermal state and the Land Surface Temperature (LST) are both significant climate variables. The latter is connected to the balance of surface energy. An estimation of the surface temperature of the planet, or the entire surface medium that the sensor views, in terms of kinetic temperature, is provided by satellite LST products down to a depth of around 12 meters (Becker & Li, 1995). Typically, the temperature of the skin is equal to the average effective radiative temperature of different soil and canopy surfaces. Skin temperature is determined by measuring the earth's surface thermal emission (Hall et al., 1992; Betts et al., 1996). LST controls upward terrestrial radiation, which regulates heat flux exchange with the atmosphere, both sensible and latent, on the surface, besides playing a crucial role in processes related to land surface (Aires et al., 2001; Sun & Pinker, 2003). Surface temperature estimation from R.S data has received a lot of attention (Li et al., 2013; Qin & Karnieli, 1999; Schmugge et al., 2002; Zhou et al., 2012; Ibraheem, 2022) for a variety of purposes, several writers have worked with remote sensing to determine LST.

Using evapotranspiration modeling as an illustration. The assessment of soil moisture (Ahmad et al., 2010; Ibraheem, 2023) as well as climate, hydrological, ecological, and biogeochemical investigations (Bhaga et al., 2020) is all dependent on knowledge of the LST. Access to accurate LST estimation at vast geographic and temporal dimensions is therefore crucial. Field measurements are practically useless for obtaining such information, however satellite thermal infrared observations are very desirable since they provide access to spatiotemporal data that is necessary for LST calculation. One of the primary prerequisites for conducting a climate change analysis is tracking changes in land cover/cover (LULC) at the regional level during a certain time period. The exchange of materials and energy between the earth's surface and lower atmosphere must be calculated, LST is the most significant environmental parameter (Feddema et al., 2005; Ibraheem & Al-Hadithi, 2024). There are several factors that impact LST that indicate that land cover change has a significant impact on the climate, such as precipitation (Joshi et al., 2020; Yagoub, 2015). Soil moisture and vegetation water stress have been measured in certain research using the vegetation index and LST (Joshi et al., 2020; Nivedha et al., 2017).

## 2. Materials and methods

### 2.1. Study area

Dahuk is in the northwest of the country of Iraq. It is situated in the center of Iraqi Kurdistan, near the meeting point of the borders of Syria, Turkey, and Iraq, giving it a strategic position. Dahuk lies surrounded by mountains, hills, and valleys. Its area (6595) km<sup>2</sup>. It takes the shape of an irregular rectangle, and passes a line 43 E. Where it extends between the eastern longitude 44° 10' E and 43° 10' E and the northern latitudes of 37° 20' and 36° 40' N as shown in Figure 1. It has a population of about 1,523,602 people.

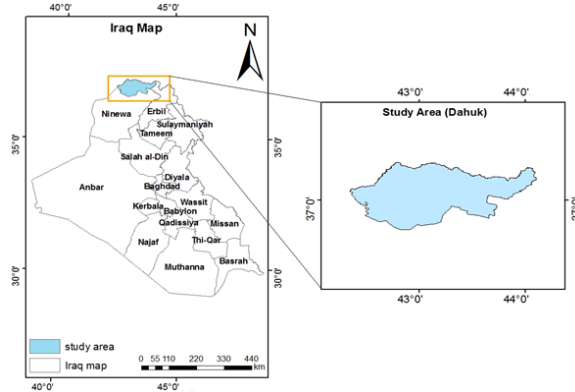


Figure 1. Location of the study area on the map

### 2.2. Data used

The first image was obtained on April 19, 2013, and the second image was obtained on April 15, 2023, both from the Landsat 8 OLI/TIRS. In this research, all bands were used, for locating LST (Table 1).

Table 1. Contains information about the remote sensing satellite data used

Bands (μm)	Landsat 8 OLI and TIRS	
	Resolution (m)	Wavelengths (μm)
Band 1-Coastal/Aerosol	30 m	0.435–0.451
Band 2/Blue	30 m	0.452–0.512
Band 3/Green	30 m	0.533–0.590
Band 4/Red	30 m	0.636–0.673
Band 5/NIR	30 m	0.851–0.879
Band 6/SWIR-1	30 m	1.566–1.651
Band 10/TIR-1	100 m	10.60–11.19
Band 11/TIR-2	100 m	11.50–12.51
Band 7/SWIR-2	30 m	2.107–2.294
Band 8/Pan	15 m	0.503–0.676
Band 9/Cirrus	30 m	1.363–1.384

## 3. Methodology

### 3.1. Pre-processing images

ArcGIS 10.3 was used to import and process images. The images were processed visually and digitally. Band 10 of

the thermal infrared spectrum was chosen for further research. The area of interest was subset from the whole sceneries using shape files.

### 3.2. Analyzing images

ArcGIS 10.3 was used in the method's construction. In this work, the Normalized Differential Vegetation Index (NDVI) was computed using bands 4 and 5, and brightness temperatures were determined using Landsat 8 Thermal Infrared bands (Band 10). The USGS webpage included the LST retrieval procedures for getting top of atmosphere (TOA) spectral radiation. Following the procedures in Figure 2, the LST was retrieved. Table 1 displays the satellite image metadata that was used in the algorithm.

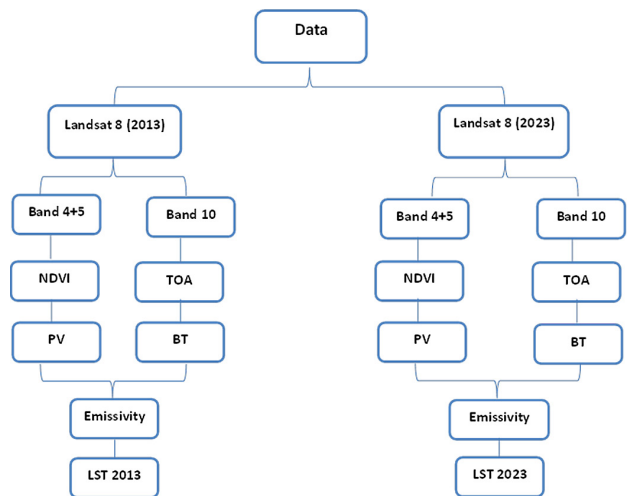


Figure 2. Methodology flowchart

### 3.3. Estimation of (LST) using Landsat 8 Satellite images

The details of the steps for estimating the LST are discussed below

#### Step 1: Transformation of digital numbers into top of atmospheric spectral radiance (TOA)

Using the radiance rescaling parameters listed in the metadata file, the Thermal band data (DN) was transformed to TOA spectral radiance (Avdan & Jovanovska, 2016).

$$L\lambda = ML \times Q_{cal} + AL, \quad (1)$$

where:  $L\lambda$  – Spectral radiance of TOA;  $ML$  – Band-specific multiplicative rescaling factor computed from metadata;  $AL$  – An additive rescaling factor particular to a band is obtained from the metadata;  $Q_{cal}$  – Standard product pixels that have been quantized and calibrated (DN).

#### Step 2: Satellite brightness temperature to TOA conversion

The thermal constants in the MTL file can be used to convert thermal band data from spectral radiance to top of atmospheric Brightness temperature.

$$BT = \frac{K2}{\ln\left(\frac{K1}{L(\lambda)} + 1\right)} - 273.15, \tag{2}$$

where: *BT* – Brightness temperature of the atmosphere; *K2* – Thermal conversion constant specific to bands from the metadata; *L* – Spectral radiance of the top of atmosphere; *K1* – Thermal conversion constant of specific band taken from metadata.

**Step 3: NDVI computation**

Based on RS data, the NDVI is produced, has a strong correlation with conditions of drought. The different visible and near-infrared wavelengths of sunlight reflected by the plants are used to determine the density of green on a given plot of land; Bands 4 and 5, which correspond to the red and near-infrared regions, were used to compute the Normal NDVI, respectively. Since the amount of vegetation present is a significant variable, estimating the NDVI is important since it may be used to infer the general status of the vegetation. Following the NDVI calculation, the vegetation proportion (PV), which is closely related to the NDVI, and emissivity ( $\epsilon$ ), which is related to the PV, should be determined. The NDVI which ranged from -1 to 1, was calculated using the differences in green vegetation’s near-infrared and red reflectance. The following formulas were used to determine the NDVI: Band 4 is the red band, or R, while Band 5 is the near-infrared band, or NIR.

$$NDVI = \frac{NIR - RED}{NIR + RED}. \tag{3}$$

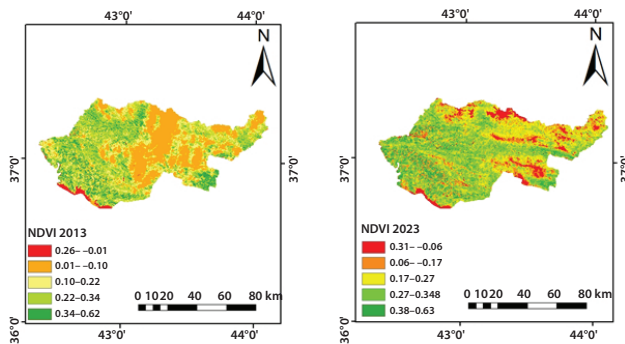


Figure 3. NDVI 2013 and 2023

**Step 4: Finding the vegetation proportion**

The percentage of the ground area covered by vegetation in a vertical projection is known as the vegetation fraction, sometimes referred to as the proportion of vegetation. When the vegetation cover changes, the land’s water and energy budgets are instantly impacted by plant transpiration, surface albedo, emissivity, and roughness (Aman et al., 1992; Ibraheem & Al-Hadithi, 2022). The NDVI values for both soil and vegetation have a strong correlation with the percentage of vegetation (Rouse et al., 1974).

$$Pv = \left( \frac{NDVI - NDVI_s}{NDVI_v - NDVI_s} \right), \tag{4}$$

NDVI<sub>v</sub> and NDVI<sub>s</sub> are the maximum and minimum NDVI values which stand for the respective NDVIs of soil and vegetation, respectively.

**Step 5: Calculating the emissivity ( $\epsilon$ )**

To calculate the emissivity, use the formula below (Sobrino et al., 2004).

$$\epsilon = 0.004 \times PV + 0.9860, \tag{5}$$

where: PV – the percentage of vegetation.

**Step 6: Land surface emissivity calculation**

Below is the LST, which has been corrected for emissivity (Stathopoulou & Cartalis, 2007):

$$T_s = \frac{BT}{1 + \left[ \left( \frac{\lambda BT}{\rho} \right) \ln \epsilon \lambda \right]}. \tag{6}$$

The emitting radiation’s wavelength,  $\lambda$ , is the LST in Celsius (for which the limiting wavelength’s average and peak responses are present). To be used is ( $\lambda = 10.895$ ) (Barsi et al., 2014a), where  $\epsilon \lambda$  is the emissivity computed in (Barsi et al., 2014b; Azua et al., 2020; Xu et al., 2004).

**4. Results and discussion**

Maps representing the study’s findings include distributions of LST, NDVI, and alterations to the study area’s land use and cover.

**4.1. Classification**

Many prior researches have employed both supervised and unsupervised classification in large amounts to create classifier maps and final output analyses. It has been noted that the majority of supervised case classifications are more accurate (Erol & Akdeniz, 1998). This study employed supervised categorization, which necessitates manual sampling for every area. High accuracy, a very low error rate, quick region classification, and area computation for each recognized region are the distinguishing features of this classification method.

This study employed supervised classification. According to the results, the area was classified into four primary classes based on the satellite images in order to show the changes in land use depicted in the maps that were created for the periods of April 2013 and April 2023 (Figure 4).

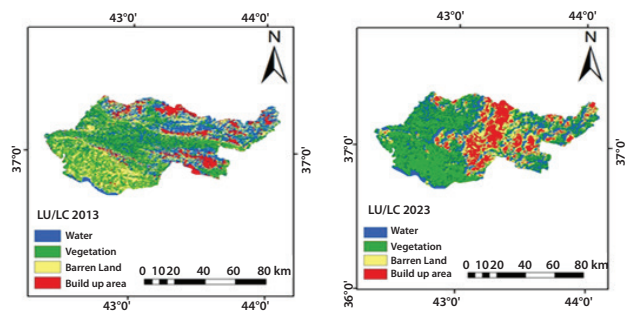


Figure 4. Supervised classification for the study area (2013 and 2023)

**Table 2.** Accuracy assessment using the selected reference pixels in 2013

Classification	Water	Vegetation	Barren land	Built up area	Total (User)
Water	9	0	0	0	9
Vegetation	0	14	3	1	18
Barren land	0	0	7	0	7
Built up area	0	0	0	12	12
Total producer	9	14	10	13	46

**Table 3.** Accuracy assessment using the selected reference pixels in 2023

Classification	Water	Vegetation	Barren land	Built up area	Total (User)
Water	7	0	0	0	7
Vegetation	0	9	0	0	9
Barren land	0	0	12	0	12
Built up area	0	2	1	3	6
Total producer	9	11	13	3	34

Water bodies, vegetated land, bare land, and built-up areas are these classes. Overall accuracy and the kappa coefficient were used to assess the accuracy of the classifications; the results were 91.1% and 91.3%, respectively. Google Earth has been used to compare the 34 reference points in 2023 and the 46 reference points in 2013 that were selected to represent various land use types with their "ground truth" Class type. The calculated total accuracy (91.3%) is higher than the Kappa value (91.1%). Differences between these two measures are to be expected, as each combines different kinds of information from the error matrix. Errors by commission and omission are not included in the overall accuracy; only data along the major diagonal is. Nevertheless, the nondiagonal components of the error matrix are included as a row and column marginal product. As shown in Tables 2 and 3.

$$\text{Overall accuracy} = \text{TCS (diagonal)} / \text{TS} \times 100; \quad (7)$$

$$\text{Kappa coefficient (T)} = (\text{TS} \times \text{TCS}) - \sum(\text{Column total} \times \text{Row total}) / \text{TS}^2 - \sum(\text{Column Total} - \text{Row Total}) \times 100, \quad (8)$$

where: TS – Total number of reference pixels; TCS – Total number of correctly classified pixels.

#### 4.2. Land use/land cover change detection

Effective community participation and management of agricultural areas has the ability to identify and recognize

changes in land use and cover. This allows monitoring changes in land use. The information on land cover that is now available aids in determining land use patterns and the variables that affect them.

By examining satellite photos, as shown in Figure 4, changes in agricultural cover, urban regions, and desolate lands between 2013 and 2023 were discovered. The area covered by buildings and barren ground increased from 17% and 15% to 42% and 27% of the entire research area, respectively, when comparing the percentage of change in land cover of the study area. In contrast, the area covered by vegetation and water have decreased from 46% and 22% to 29% and 2% as shown in Figure 5 and Table 4.

Table 4 representative of the research area's whole LULC area, which is about (6595) km<sup>2</sup>. Particularly in urban areas where they have greatly increased, LULC has grown. Table 4 shows that between 2013 and 2023, the building types have a big growth from (998.08) km<sup>2</sup> to (1767.79) km<sup>2</sup>. The barren area increased from (1125.5 km<sup>2</sup> to 2743.3 km<sup>2</sup>) through the years 2013–2023, whereas the area covered by water increased from (1417.04 km<sup>2</sup> to 166.31 km<sup>2</sup>) through the years 2013–2023. Vegetation area decreased from (3054.38 km<sup>2</sup> to 1917.6 km<sup>2</sup>), respectively from 2013 to 2023, as shown in table below.

**Table 4.** The different land uses and regions in the research area between 2013 and 2023

Type of use	2013		2023		Change detection	
	Area km <sup>2</sup>	Area %	Area km <sup>2</sup>	Area %	Area km <sup>2</sup>	Area %
Water	1417.04	22%	166.31	2%	-1250.73	-20%
Vegetation	3054.38	46%	1917.6	29%	-1136.78	-17%
Barren land	1125.5	17%	2743.3	42%	1617.8	25%
Build up area	998.08	15%	1767.79	27%	769.71	12%
Total	6595	100%	6595	100%		

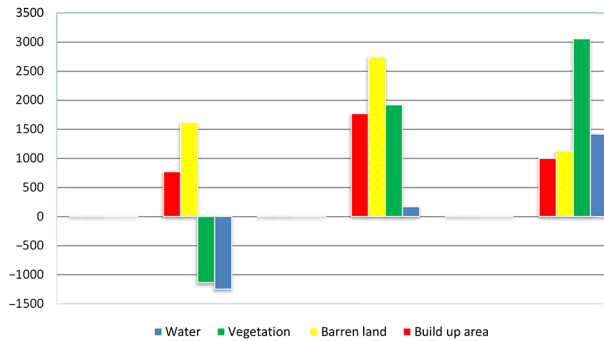


**Figure 5.** Percentage change of land use land cover categories for the period of 2013 and 2023

### 4.3. Land surface temperature map

The study area absolute LST map is the research's output for the study region. In Figure 3, the resulting LST map is displayed. Temperature ranges reported by LST readings in 2013 and 2023 were (4–14) and (10–20) degrees Celsius, respectively. For the entire region, the maximum LST rose by 6 °C from 14 °C in 2013 and 20 °C in 2023. Simultaneously, the minimum temperature rose to 6 °C from 4 °C to 10 °C, as showing in Figure 4. The 2013 images were taken on April 19, 2014 and the 2023 images on April 15, 2023. Possible climate change effects include these changes.

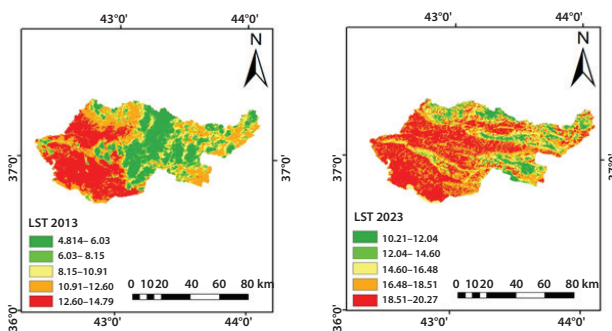


**Figure 6.** LST 2013 and 2023

Figure 6 shows the location of the LST in Dahuk City, the LST values ranged between (4–14) and (10–20) °C. A variety of LULC categories, such as water bodies, greenery, wasteland, and high-rise buildings are dispersed over huge areas present throughout the city. The majority of the research region is high mountainous terrain where temperatures are lower, like the 4 and 10 °C that were recorded there.

## 5. Conclusions

This study used multi-temporal remote sensing data to monitor changes in land use and land cover and how they affect LST in Dahuk Governorate. The strategies employed in this inquiry to accomplish the goals of the study proved effective. The aim of the study was to determine the impact of changes in land use categories on LST. Dry ground, urban

areas, water bodies, and vegetated regions were separated from the research area. Political and socioeconomic forces reduced the size of water bodies and increased the growth of building areas, whereas vegetation and arid land reduced during the course of the research period. It is clear that there is a connection between LST and LULC. The study demonstrated that as LST values fluctuate, so do the various classifications of land cover; For example, vegetation areas and water bodies were high in 2013 when temperatures were low while the percentage of those areas decreased when temperatures increased in 2023.

## References

- Ahmad, S., Kalra, A., & Stephen, H. (2010). Estimating soil moisture using remote sensing data: A machine learning approach. *Advances in Water Resources*, 33(1), 69–80. <https://doi.org/10.1016/j.advwatres.2009.10.008>
- Aires, F., Prigent, C., Rossow, W. B., & Rothstein, M. (2001). A new neural network approach including first-guess for retrieval of atmospheric water vapor, cloud liquid water path, surface temperature and emissivities over land from satellite microwave observations. *Journal of Geophysical Research*, 106, 14887–14907. <https://doi.org/10.1029/2001JD900085>
- Aman, A., Randriamanantena, H. P., Podaire, A., & Frouin, R. (1992). Upscale integration of normalized difference vegetation index: The problem of spatial heterogeneity. *IEEE Transactions on Geoscience and Remote Sensing*, 30, 326–338. <https://doi.org/10.1109/36.134082>
- Avdan, U., & Jovanovska, J. (2016). Algorithm for automated mapping of land surface temperature using LANDSAT 8 satellite data. *Journal of Sensors*, 2016(1), Article 1480307. <https://doi.org/10.1155/2016/1480307>
- Azua, S., Nnah, S. I., & Ikwueze, H. U. (2020). Spatio-temporal variability of landuse landcover and its impact on land surface temperature in Zaria Metropolis, Nigeria. *FUTY Journal of the Environment*, 14, 1–11.
- Barsi, J. A., Lee, K., Kvaran, G., Markham, B. L., & Pedelty, J. A. (2014a). The spectral response of the Landsat-8 operational land imager. *Remote Sensing*, 6(10), 10232–10251. <https://doi.org/10.3390/rs61010232>
- Barsi, J. A., Schott, J. R., Hook, S. J., Raqueno, N. G., Markham, B. L., & Radocinski, R. G. (2014b). Landsat-8 Thermal Infrared Sensor (TIRS) vicarious radiometric calibration. *Remote Sensing*, 6(11), 11607–11626. <https://doi.org/10.3390/rs61111607>
- Becker, F., & Li, Z.-L. (1995). Towards a local split window method over land surface. *International Journal of Remote Sensing*, 3, 17–33.
- Betts, A. K., Ball, J. H., Beljaars, A. C. M., Miller, M. J., & Viterbo, P. A. (1996). The land surface-atmosphere interaction: A review based on observational and global modeling perspectives. *Journal of Geophysical Research*, 101, 7209–7225. <https://doi.org/10.1029/95JD02135>
- Bhaga, T. D., Dube, T., Shekede, M. D., & Shoko, C. (2020). Impacts of climate variability and drought on surface water resources in sub-Saharan Africa using remote sensing: A review. *Remote Sensing*, 12(24), Article 4184. <https://doi.org/10.3390/rs12244184>
- Erol, H., & Akdeniz, F. (1998). A new supervised classification method for quantitative analysis of remotely-sensed multi-spectral data. *International Journal of Remote Sensing*, 19(4), 775–782. <https://doi.org/10.1080/014311698216008>

- Feddema, J. J., Oleson, K. W., Bonan, G. B., Mearns, L. O., Buja, L. E., Meehl, G. A., & Washington, W. M. (2005). The importance of land-cover change in simulating future climates. *Science*, 310(5754), 1674–1678. <https://doi.org/10.1126/science.1118160>
- Hall, F. G., Huemmrich, K. F., Goetz, S. J., Sellers, P. J., & Nickerson, J. E. (1992). Satellite remote sensing of surface energy balance: Success, failures, and unresolved issues in FIFE. *Journal of Geophysical Research*, 97, 19061–19089. <https://doi.org/10.1029/92JD02189>
- Ibraheem, I. F. (2022). Remote sensing application for the assessment of urban heat island development in Baghdad, Iraq. *International Journal of Advances in Engineering and Emerging Technology*, 13(2), 182–192.
- Ibraheem, I. F. (2023). Remote sensing data and environmental parameters usage for the establishment of a mapping of solar energy potential in Iraq. *AIP Conference Proceedings*, 2787(1), Article 080032. <https://doi.org/10.1063/5.0149069>
- Ibraheem, I. F., & Al-Hadithi, M. (2022). Remote sensing utilization for the modelling of land surface temperature for sustainable city development. *Open Access Repository*, 8(7), 95–106. <https://doi.org/10.17605/OSF.IO/3AVNW>
- Ibraheem, I. F., & Al-Hadithi, M. (2024). Application of remote sensing and GIS techniques in integrated management of changes in LU\LC and effective community participation in Baghdad-Aldora. *AIP Conference Proceedings*, 3105(1), Article 050092. <https://doi.org/10.1063/5.0212230>
- Joshi, R. C., Ryu, D., Sheridan, G. J., & Lane, P. N. J. (2020, May 4–8). A new remote sensing-based vegetation water stress index: Temperature Vegetation Water Stress Index (TVWSI) [Online]. EGU General Assembly. <https://doi.org/10.5194/egusphere-egu2020-12308>
- Li, Z. L., Tang, B., & Wu, H. (2013). Satellite-derived land surface temperature: Current status and perspectives. *Remote Sensing of Environment*, 131, 14–37. <https://doi.org/10.1016/j.rse.2012.12.008>
- Nivedha, D. S., Jasminenketha, M., Geetha, P., & Soman, K. P. (2017). Agricultural drought analysis for Thuraiyur taluk of Tiruchirappalli District using NDVI and land surface temperature data. In *11th International Conference on Intelligent Systems and Control (ISCO)* (pp. 155–159). Coimbatore. <https://doi.org/10.1109/ISCO.2017.7855972>
- Qin, Z., & Karnieli, A. (1999). Progress in remote sensing of land surface temperature and ground emissivity using NOAA-AVHRR data. *International Journal of Remote Sensing*, 20(12), 2367–2393. <https://doi.org/10.1080/014311699212074>
- Rouse, J. W., Jr., Haas, R. W., Schell, J. A., Deering, D. W., & Harlan, J. C. (1974). *Monitoring the vernal advancement and retrogradation (green wave effect) of natural vegetation* (NASA / GSFC Type III Final Report). Texas A&M University, Remote Sensing Center, College Station.
- Schmugge, T. J., Kustas, W. P., Ritchie, J. C., Jackson, T. J., & Rango, A. (2002). Remote sensing in hydrology. *Advances in Water Resources*, 25(8–12), 1367–1385. [https://doi.org/10.1016/S0309-1708\(02\)00065-9](https://doi.org/10.1016/S0309-1708(02)00065-9)
- Sobrinho, J. A., Jiménez-Muñoz, J. C., & Paolini, L. (2004). Land surface temperature retrieval from LANDSAT TM5. *Remote Sensing of Environment*, 90(4), 434–440. <https://doi.org/10.1016/j.rse.2004.02.003>
- Stathopoulou, M., & Cartalis, C. (2007). Daytime urban heat islands from Landsat ETM+ and Corine land cover data: An application to major cities in Greece. *Solar Energy*, 81(3), 358–368. <https://doi.org/10.1016/j.solener.2006.06.014>
- Sun, D., & Pinker, R. T. (2003). Estimation of land surface temperature from a Geostationary Operational Environmental Satellite (GOES-8). *Journal of Geophysical Research*, 108, 4326–4241. <https://doi.org/10.1029/2002JD002422>
- Xu, H. Q., & Chen, B. Q. (2004). Remote sensing of the urban heat island and its changes in Xiamen City of SE China. *Journal of Environmental Sciences*, 16, 276–281.
- Yagoub, H. (2015). *Cartographie et suivi du couvert végétal des zones semi-arides par l'imagerie satellitaire* [Mapping and monitoring of vegetation cover in areas semi-arid by satellite imagery] [Thesis]. Université des Sciences et de la Technologie d'Oran Mohamed Boudiaf, Faculté de Physique.
- Zhou, J., Li, J., Zhang, Li., Hu, D., & Zhan, W. (2012). Intercomparison of methods for estimating land surface temperature from Landsat-5 TM image in an arid region with low water vapor in the atmosphere. *International Journal of Remote Sensing*, 33(8), 2582–2602. <https://doi.org/10.1080/01431161.2011.617396>